DIRECT NUMERICAL SIMULATION OF THE ROTATING DISK TURBULENT BOUNDARY LAYER

Nicholas Morse[1]
[1]FLOW, Department of Engineering Mechanics
KTH Royal Institute of Technology
100 44 Stockholm, Sweden
morse@kth.se

Niclas Jansson[2]
[2]KTH Center for Scientific Computing
KTH Royal Institute of Technology
100 44 Stockholm, Sweden
njansson@kth.se

Mathis Bode[3]
[3]Jülich Supercomputing Centre
Forschungszentrum Jülich GmbH
52428 Jülich, Germany
m.bode@fz-juelich.de

R.J. Lingwood[1,4]
[4]School of Engineering
Lancaster University
LA1 4YR Lancaster, United Kingdom
r.lingwood@lancaster.ac.uk

P. Henrik Alfredsson[1]
[1]FLOW, Department of Engineering Mechanics
KTH Royal Institute of Technology
100 44 Stockholm, Sweden
hal@kth.se

Mihai Mihaescu[1]
[1]FLOW, Department of Engineering Mechanics
KTH Royal Institute of Technology
100 44 Stockholm, Sweden
mihaescu@kth.se

Ramis Örlü[1,5]
[5]Dept. of Mechanical, Electrical and Chemical Eng.
OsloMet – Oslo Metropolitan University
0166 Oslo, Norway
ramis.orlu@oslomet.no

Philipp Schlatter[1,6]
[6]Institute of Fluid Mechanics (LSTM)
Friedrich–Alexander–Universität (FAU)
91058 Erlangen–Nürnberg, Germany
philipp.schlatter@fau.de

ABSTRACT

The von Kármán turbulent boundary layer (vKTBL) induced by a rotating disk is a canonical three-dimensional turbulent boundary layer (3DTBL) that develops without a 2D precursor and exhibits unique structural features, including discrepancies between momentum and heat transfer. We present direct numerical simulations (DNS) of the vKTBL up to an azimuthal friction Reynolds number of 2300, higher than any previous DNS, enabled by a GPU-accelerated spectral element method. We also perform the first DNS of the disk's thermal boundary layer. The results for unity Prandtl number confirm experimental observations in air of a wake component in the mean temperature profile, which is not present in the velocity profile. The DNS highlights structural similarities and differences relative to 2DTBLs, providing new insights into turbulence and scalar transport in 3DTBLs.

INTRODUCTION

Three-dimensional turbulent boundary layers (3DTBLs) are ubiquitous in both geophysical and engineering applications (e.g., the atmospheric boundary layer, swept wings, junction flows, compressor or turbine blades), but have received less attention than their two-dimensional counterparts (2DTBLs). Recently, a renewed interest in 3DTBLs has emerged, aiming at improving the accuracy of wall-modeled large-eddy simulation (WMLES). Additionally, advancements in computational power have enabled direct numerical simulations (DNS) of 3DTBLs at ever-increasing Reynolds numbers, providing an avenue towards a structural understanding of 3DTBLs on par with the well-established history of 2DTBL research. The heat or scalar transport of such 3DTBLs is also relevant to geophysical and turbomachinery applications, but has received even less attention than momentum transport.

The flow induced by a rotating disk is a canonical example of a 3D boundary layer, with a laminar similarity solution derived by von Kármán (1921) and a corresponding thermal boundary layer solution by Millsaps & Pohlhausen (1952). Owing to its relative simplicity and similarity of its cross-flow instability to swept-wing boundary layers, the rotating disk boundary layer has been the subject of numerous experimental and stability studies (Alfredsson *et al.*, 2024). Its turbulent counterpart, the von Kármán turbulent boundary layer (vKTBL), may be classified with other viscous-driven 3DTBLs (Lozano-Durán *et al.*, 2020), although it has several unique characteristics. The vKTBL, continuously forced by disk rotation, is inherently three-dimensional, and reaches equilibrium without any transitional history from a 2DTBL. Due to its statistical axisymmetry, its mean flow can be described using only two spatial coordinates (r, z, i.e. the radial and wall-normal directions), offering an opportunity to study 3DTBL and Coriolis effects in a simplified setting.

Despite these characteristics, the vKTBL has only been studied numerically by a single DNS (Appelquist *et al.*, 2018) and a large-eddy simulation (LES) (Wu & Squires, 2000). Relatively few experiments have investigated the vKTBL, perhaps due to difficulties with near-wall measurements and surface roughness, since (unlike 2DTBLs) the viscous length scale decreases strongly with r. Additionally, the near-zero velocity magnitude near the edge of the boundary layer for the disk rotating in the laboratory frame makes it difficult to measure outer scales. Despite these challenges, existing literature has revealed several noteworthy features of the vKTBL, the most striking being the absence of a wake region in the mean velocity profile. However, a prominent wake has been observed experimentally in the temperature profile (Elkins & Eaton, 2000), indicating a structural dissimilarity between momentum and heat transfer in the vKTBL that is absent in 2DTBLs.

Many questions remain regarding the structure of turbulence and heat transfer in the vKTBL, motivating the present study. We leverage modern hardware accelerators to perform a DNS of the vKTBL, reaching friction Reynolds numbers, $Re_\tau = \delta_{99}/\ell_\star$ (based on the 99% boundary-layer thickness, δ_{99}, and viscous length scale, $\ell_\star = \nu^*/v^*_\tau$, where ν^* is the kinematic viscosity and v^*_τ is the friction velocity in the azimuthal direction), of up to 2300, approximately 2.5 times higher than prior DNS (Appelquist *et al.*, 2018). We also report the first DNS of the disk's thermal boundary layer by simulating the transport of a passive scalar with unity Prandtl number (ratio of momentum to thermal diffusivity). In the following, we detail the numerical method and computational setup for the present simulations, with specific consideration of boundary conditions, domain size, and grid resolution. Finally, we present statistics of wall and integral quantities from the present DNS, along with profiles of mean and turbulent quantities for both velocity and temperature.

SIMULATION DETAILS

We simulate a disk rotating in a still fluid with angular velocity Ω^*, such that the local wall velocity is $V^*_w = \Omega^* r^*$, where starred variables are dimensional. Lengths are non-dimensionalized using the von Kármán viscous length scale, $\delta^* = \sqrt{\nu^*/\Omega^*}$, such that, e.g., $r = r^*/\delta^*$. In the simulation, velocities are normalized by the disk edge velocity, $V^*_{w,\mathrm{edge}} = \Omega^* r^*_{\mathrm{edge}}$, so that the maximum velocity difference across the boundary layer is one. The temperature is non-dimensionalized as $\phi = (\phi^* - \Phi^*_\infty)/(\Phi^*_w - \Phi^*_\infty)$, where Φ^*_w and Φ^*_∞ denote the disk and ambient temperatures, respectively.

The present DNS is performed using the open-source solver *Neko* (Jansson *et al.*, 2024), a spectral element method written in modern Fortran with backends for various accelerators. We advance the incompressible Navier–Stokes equations

$$\frac{\partial u_i}{\partial t} + u_j \frac{\partial u_i}{\partial x_j} = -\frac{\partial p}{\partial x_i} + \frac{1}{Re}\frac{\partial^2 u_i}{\partial x_j \partial x_j} + f_i\ , \tag{1}$$

$$\frac{\partial u_i}{\partial x_i} = 0\ , \tag{2}$$

where $Re = V^*_{w,\mathrm{edge}}\delta^*/\nu^* = 1200$ is the simulation Reynolds number and f_i is an optional forcing term. The solution is integrated using third-order semi-implicit time advancement, where velocity and pressure are discretized using 7th-order spatial polynomials in the P_N–P_N formulation. The temperature is treated as a passive scalar, which is appropriate given the approximately 10°C difference between the disk and ambient temperatures in the reference experiments (Elkins & Eaton, 2000). The temperature equation is therefore

$$\frac{\partial \phi}{\partial t} + u_j \frac{\partial \phi}{\partial x_j} = \frac{1}{Re\,Pr}\frac{\partial^2 \phi}{\partial x_j \partial x_j}\ , \tag{3}$$

where we choose a Prandtl number of unity ($Pr = 1$).

Domain and Grid Sizing

The computational domain is an annular sector (Figure 1), defined in cylindrical coordinates by $r \in [r_{\mathrm{inflow}}, r_{\mathrm{outflow}}]$, $\theta \in [0, L_\theta]$, and $z \in [0, L_z]$. The inflow radius, $r_{\mathrm{inflow}} \approx 363$, is selected such that it is below the natural transition point of the boundary layer to facilitate comparison with experiments, while the outer radius of the disk, $r_{\mathrm{edge}} = 1200$, is determined by the desired local Reynolds number, which is quadratic in r: $Re_r = r^* V^*_w/\nu^* = r^2$. Past the disk edge, the bottom wall is changed to a slip wall and a weak sponge is used to drive u_θ to zero (similar to Appelquist *et al.* (2018)) before the outflow boundary at $r_{\mathrm{outflow}} \approx 1308$, which is placed sufficiently far from r_{edge} as to not influence the flow over the disk. The sponge suppresses turbulence past the disk edge, allowing for radial coarsening of the grid before the outflow boundary. The other extents of the domain, L_θ and L_z, are selected based on a fit to published experimental measurements of $\delta_{99}(r)$ for the vKTBL, such that $\min(rL_\theta/\delta_{99}(r)) > 22.6$ and $\min(L_z/\delta_{99}(r)) > 3$ throughout the domain.

Likewise, the near-wall grid spacings are determined based on a power-law fit of published experimental measurements of the viscous length scale, $\ell_\star(r)$, in the vKTBL. Since $\ell_\star$ decreases with r, such that inner-layer resolution requirements are most restrictive at r_{edge}, the element spacings Δ_z and Δ_θ are fixed by $\ell_\star(r_{\mathrm{edge}})$, while the radial element spacing is allowed to vary with r as $\Delta_r(r) \propto \ell_\star(r)$ to maintain a constant radial resolution in wall units, Δ_r^+. Throughout the paper, plus superscripts ($^+$) correspond to normalization using wall quantities ($\ell_\star$ and v_τ) based on the azimuthal wall shear stress. The element spacing in z is designed to follow the suggestions of Pirozzoli & Orlandi (2021), based on the estimated Kolmogorov scale in the logarithmic layer. The first Gauss-Lobatto-Legendre (GLL) point is always located below $z^+ = 0.1$, with 64 points below $z^+ = 50$. The element spacing $\Delta_r(r)$ varies with r to maintain $(\Delta_r(r)/P)^+ \approx 5$, where $P = 7$ is the spatial polynomial order. The azimuthal spacing is selected based on the most restrictive requirement at r_{edge} such that $1.75 < (r\Delta_\theta/P)^+ \leq 10$ within the TBL (becoming more refined at lower r). For $r < r_{\mathrm{trip}}$, $r > r_{\mathrm{edge}}$, and $z > \max(\delta_{99})$, geometric growth rates are applied to the element spacings to limit the computational cost. In total, the grid comprises 52 million spectral elements, corresponding to 17.9 billion unique GLL points, partitioned across 3072 NVIDIA GH200 superchips on Forschungzentrum Jülich's JUPITER supercomputer.

Boundary Conditions and Tripping

Referencing Figure 1, the fluid and thermal boundary conditions are as follows. At $z = 0$, a no-slip, isothermal boundary is applied by setting $u_\theta = \Omega r$ and $\phi = 1$. Cyclic periodic boundary conditions are employed in the θ-direction, which is appropriate due to the statistical homogeneity of the flow in

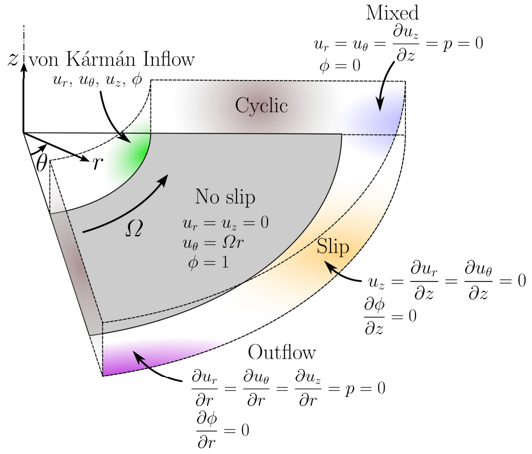

Figure 1. A sketch of the computational domain, coordinate system, and boundary conditions, not drawn to scale.

this direction. At the inner radial boundary, an inflow Dirichlet boundary condition sets the laminar similarity solutions for the velocity (von Kármán, 1921) and temperature (Millsaps & Pohlhausen, 1952), which are also used as the initial condition. Special treatment is required for the outer radial boundary. The velocity boundary condition is a natural outflow treated with the stabilization method of Dong *et al.* (2014), with a Neumann condition applied for the scalar ($\partial\phi/\partial r = 0$). Finally, on the top boundary, a mixed boundary condition is enforced to set $\partial u_z/\partial z$, u_r, u_θ, and ϕ to zero, allowing the entrainment velocity (u_z) to adjust to the development of the boundary layer.

The boundary layer is tripped using a weak, random volume force acting in the z direction, following Schlatter & Örlü (2012). The forcing spans the θ extent of the domain, with a field defined by a Gaussian function centered about $(r, z) = (430,\, 0)$ with standard deviations $(\sigma_r,\, \sigma_z) = (4\delta_1,\, \delta_1)$, where $\delta_1 = 1.2$ is the displacement thickness of the laminar von Kármán boundary layer. The number of modes in the azimuthal direction is selected as approximately $r_{\text{trip}} L_\theta/\sigma_r$, with a time scale $\sigma_r/(\Omega r_{\text{trip}})$ and amplitude $20\Omega^2 r_{\text{trip}}$. For further details on tripping parameters, see Schlatter & Örlü (2012).

The laminar initial condition is tripped and the simulation is allowed to evolve for a transient period of 1.3 disk rotations before statistics are collected for an additional 2.4 rotations.

RESULTS

Contours of the instantaneous scalar field on planes at $z = 0.2$ (approximately $4 < z^+ < 10$) and $z = 10$ ($z/\delta_{99} > 0.2$) are shown in Figures 2*a* and 2*b*, along with a θ-slice of the same field in Figure 2*c*. The top-down view in the near-wall region (Figure 2*a*) reveals the presence of the characteristic streaks of the inner layer in wall-bounded turbulence. These streaks appear more disorganized than those in 2DTBLs due to the strong cross-flow component, and the streak spacing can be seen to narrow with r, in accordance with the radial decrease of $\ell_\star$. In contrast, the scalar field in the outer region (Figure 2*b*) displays significantly larger and more incoherent turbulent motions that are less well aligned with the azimuthal direction. The θ cross-section in Figure 2*c* illustrates the spatial growth of the TBL in the radial direction past the tripping location and its sharp interface with the quiescent ambient. In the laminar region before the trip, the boundary-layer thickness is constant in r, in accordance with the similarity solution. In contrast with 2DTBLs, the primary velocity is not in the direction of the boundary-layer growth, so the cross-section in Figure 2*c* appears more similar to a streamwise cross-section of a 2DTBL, without the ramp-like structures typical of spanwise 2DTBL visualizations. These structures do, however, appear in the azimuthal direction.

Integral and Global Quantities

Figure 3 shows the evolution of $\ell_\star = \nu^*/v_\tau^*$ and $Re_\tau = \delta_{99}/\ell_\star$ from the present DNS versus r, along with data from published DNS and experiments (symbols). Also shown in dotted lines is the evolution of $\ell_\star$ from the laminar similarity solution, and a turbulent correlation for $\ell_\star$ from the vKTBL azimuthal skin friction correlation of von Kármán (1921). The radial decrease of $\ell_\star$ is evident, and the present DNS matches well with the published data in both the laminar and turbulent regimes. The sharper drop of $\ell_\star$ at the tripping location ($r = 430$) compared to Appelquist *et al.* (2018) is due to differences in the tripping parameters. The turbulent correlation of von Kármán (1921) predicts the turbulent regime remarkably well.

The radial decrease of $\ell_\star$ contributes to the increase of Re_τ across the disk, which reaches a maximum value of approximately 2300 by the disk edge in the present DNS. We find that our Re_τ agrees well with Imayama *et al.* (2014), Digre (2015), and Mollaei *et al.* (2024), but remains lower than Littell & Eaton (1994), despite a good collapse of the experimental and DNS data for $\ell_\star$. This discrepancy is therefore likely due to the difficulty of measuring the 99% boundary-layer thickness in experiments due to the nearly still fluid away from the disk, as mentioned as a note of caution in Littell & Eaton (1994).

Figure 4 shows the azimuthal and radial skin friction coefficients, which are given by $C_{f,\theta} = \tau_{w,\theta}/\frac{1}{2}\rho V_w^2$ and $C_{f,r} = \tau_{w,r}/\frac{1}{2}\rho V_w^2$, where ρ is the density and $\tau_{w,\theta}$ and $\tau_{w,r}$ are the components of the wall shear stress in the azimuthal and radial directions, respectively. In Figure 4, we find that the azimuthal skin friction increases post-transition, while the radial skin friction decreases below its laminar value. Both skin friction components decrease at a slower rate in the turbulent region than in the laminar region, while the angle formed by the radial and azimuthal skin friction coefficients ($\text{atan}(C_{f,r}/C_{f,\theta})$) was found to decrease slowly with r from a value of around 20° post-transition to less than 14° by $r = 1200$.

In Figure 5, we show the evolution of the displacement and momentum thicknesses of the vKTBL, defined as

$$\delta_1 = \int_0^{\delta_{99}} \frac{V}{V_w}\,\mathrm{d}z \tag{4}$$

$$\delta_2 = \int_0^{\delta_{99}} \frac{V}{V_w}\left(1 - \frac{V}{V_w}\right)\mathrm{d}z \tag{5}$$

Before the trip, δ_1 and δ_2 are constant in r, and agree well with the result of the similarity solution (dotted lines). At larger radii, well after the tripping location, δ_1 and δ_2 increase together, leading to a slow decline of the shape factor, $H = \delta_1/\delta_2$ seen in Figure 6. The ratio δ_{99}/δ_1 in Figure 6 increases with r, exceeding 9 by the edge of the disk. As reported in Mollaei *et al.* (2024), this value is larger than typical values for 2DTBLs; cf. Schlatter & Örlü (2012).

Mean and Turbulence Profiles

Profiles of the mean wall-parallel velocities and temperature in wall units (based on $\tau_{w,\theta}$) are shown in Figure 7 at three different radii, with data from Imayama *et al.* (2014) and

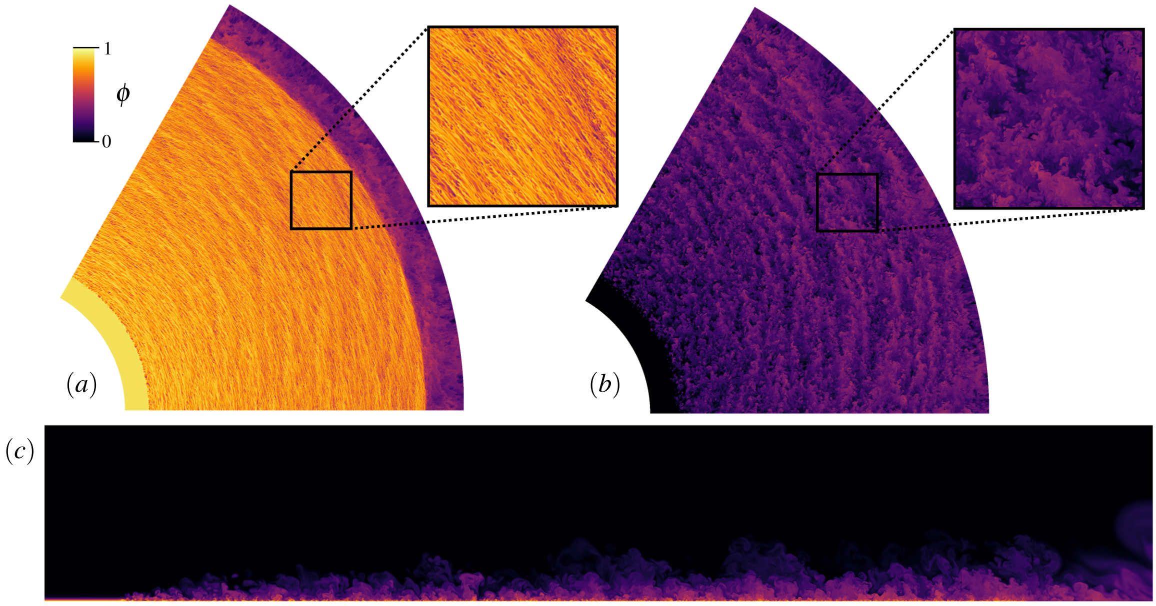

Figure 2. Top-down ($-z$) views of the instantaneous ϕ field on slices of the flow field at $z = 0.2$ (a) and $z = 10$ (b), where the disk rotates counter-clockwise. Also shown is a θ-slice (c) of the same field.

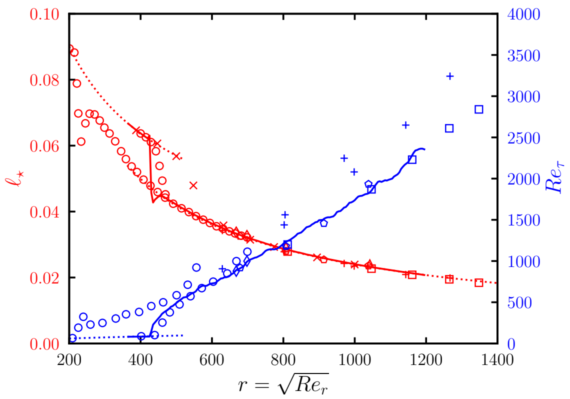

Figure 3. Viscous length scale ($\ell_\star$) and friction Reynolds number (Re_τ) from the present DNS (solid lines) and published experiments and DNS (symbols): Itoh & Hasegawa (1994) ($\times$), Littell & Eaton (1994) ($+$), Elkins & Eaton (2000) ($\triangle$), Imayama *et al.* (2014) ($\diamondsuit$), Digre (2015) (⬠), Appelquist *et al.* (2018) ($\bigcirc$), and Mollaei *et al.* (2024) ($\square$). A laminar curve for Re_τ and laminar and turbulent curves for $\ell_\star$ based on the laminar similarity solution and turbulent correlation of von Kármán (1921) are also shown (dotted lines).

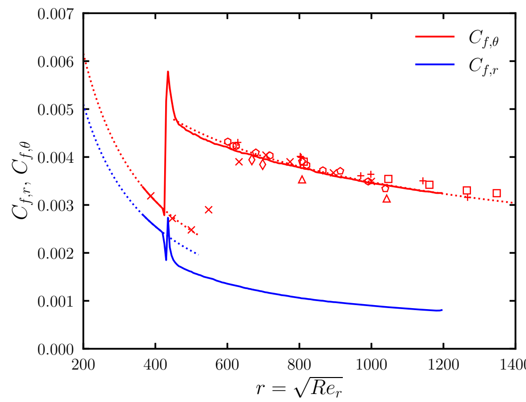

Figure 4. Azimuthal and radial skin friction coefficients, $C_{f,\theta}$ and $C_{f,r}$, from the present DNS (solid lines) compared to published data (symbols, as in Figure 3) and the laminar similarity solution and turbulent correlation of von Kármán (1921) (dotted lines).

Appelquist *et al.* (2018) provided for comparison at the lowest radius. We follow the notation of Alfredsson *et al.* (2024) and much past vKTBL work by designating velocities in the r, θ, and z directions as U, V, and W, respectively, such that the primary velocity component is V. Reynolds decompositions of the solution variables are employed ($u_i = U_i + u_i'$, $\phi = \Phi + \phi'$), where capital letters denote mean values, primes denote fluctuating quantities, and (time and azimuthal) averages are represented with overbars. The profiles for the mean azimuthal velocity in the disk frame, $(V_w - V)^+$, confirm the near absence of a wake, which has been reported in past vKTBL literature and bears similarities to suction TBLs, see e.g. Bobke *et al.* (2016). In contrast, the mean temperature profile exhibits a significant wake, which was observed in the experiments of Elkins & Eaton (2000) in air ($Pr = 0.71$). In the present DNS, we find that the wake component persists in magnitude until the largest r of the simulation.

In Figure 8, the profiles of the Reynolds normal stresses, turbulent kinetic energy (TKE), scalar variance, and turbulent scalar fluxes are presented in wall units. The normal stresses (Figure 8a) show a dominant azimuthal component $\overline{v'^2}$, with a peak occurring near $z^+ \approx 15$. Since the wall-normal gradient of azimuthal velocity dominates, $\overline{v'^2}$ exceeds $\overline{u'^2}$, making the TKE (k) largely driven by azimuthal fluctuations. In each of the Reynolds stresses, we observe good agreement with the DNS of Appelquist *et al.* (2018) at the first station.

In Figure 8b, the scalar variance $\overline{\phi'^2}$ exhibits a prominent primary peak in the inner layer, similar to the TKE. However, in contrast to Elkins & Eaton (2000), no second peak in the

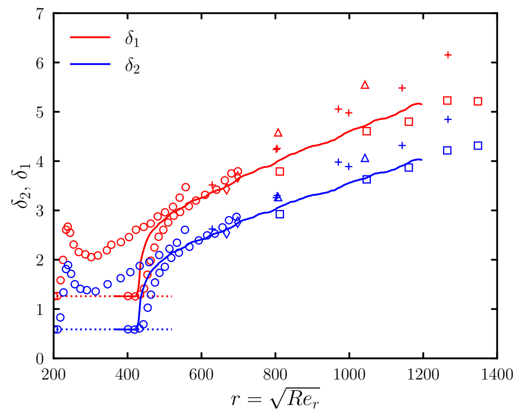

Figure 5. Boundary-layer displacement and momentum thicknesses, δ_1 and δ_2, from the present DNS (solid lines), published data (symbols, as defined in Figure 3), and for the laminar similarity solution (dotted lines).

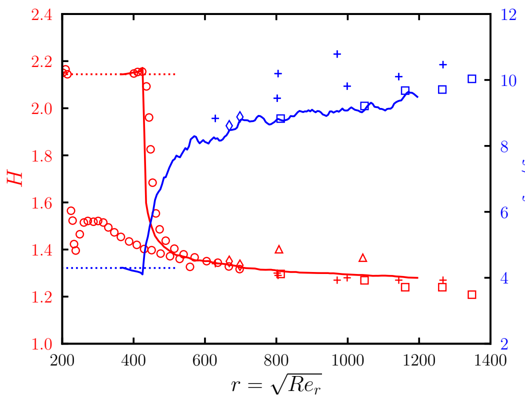

Figure 6. Shape factor, $H = \delta_1/\delta_2$, and δ_{99}/δ_1 ratio from the present DNS, plotted alongside published DNS and experimental data, with symbols as described in Figure 3.

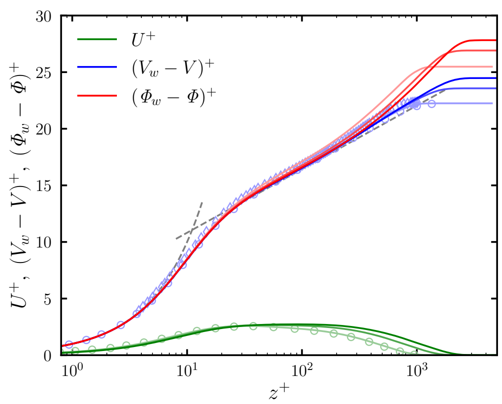

Figure 7. Profiles of the mean azimuthal velocity (blue), radial velocity (green), and temperature (red) in inner units. Profiles at $r = 668$, 900, 1000 are shown in light to dark colors. Data from Imayama *et al.* (2014) ($\Diamond$) and Appelquist *et al.* (2018) ($\bigcirc$) from $r = 668$ are provided for comparison. Dashed lines for the linear-law ($(V_w - V)^+ = z^+$) and log-law ($(V_w - V)^+ = \kappa^{-1} \ln z^+ + B$, with $\kappa = 0.41$ and $B = 5.2$) are shown.

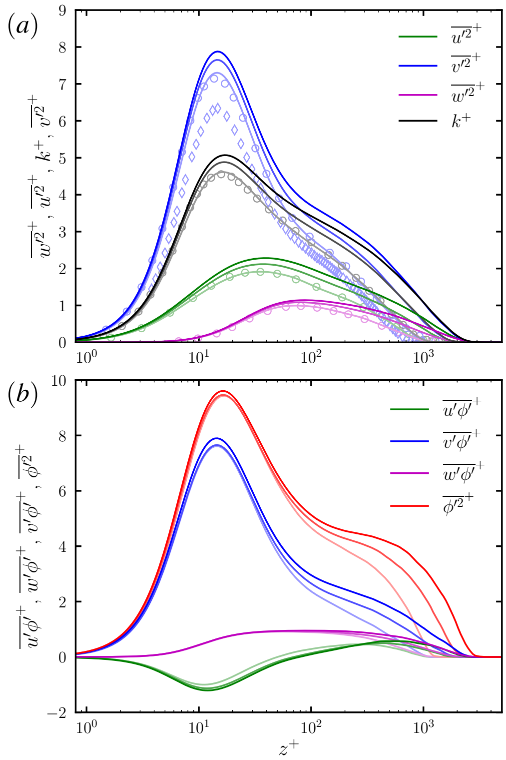

Figure 8. Profiles of Reynolds normal stresses and TKE (*a*) and scalar variance and turbulent fluxes (*b*). Also plotted are the data at $r = 668$ from Imayama *et al.* (2014) ($\Diamond$) and Appelquist *et al.* (2018) ($\bigcirc$). Line shades correspond to stations described in Figure 7.

outer layer is found. This seems to confirm their hypothesis that this observation was an experimental artifact due to the elevated wall temperature in the laminar region, which heated fluid that was subsequently expelled away from the wall after transition. However, unlike the velocity statistics, there is a prominent shoulder of $\overline{\phi'^2}$ in the outer region ($z^+ > 100$), which grows stronger with increasing Reynolds number. This structural difference suggests that while the near-wall dynamics of the passive scalar fluctuations follows the momentum transport, the outer-layer dynamics of the passive scalar are governed by a different set of mechanisms, likely linked to the prominent wake component observed in the mean scalar profile. Hence, a similar shoulder is not observed in either the turbulent scalar flux or Reynolds normal stress components, due to the absence of the wake in the azimuthal velocity profile.

In their reasoning about the outer peak of $\overline{\phi'^2}$ in their rotating disk experiments, Elkins & Eaton (2000) suggested that it must be due to heated fluid being transported outward as the boundary layer develops, since there is no outer peak in the production of $\overline{\phi'^2}$. In Figure 9, we plot the production and premultiplied production of k and $\overline{\phi'^2}$ for the same radial stations shown in figures 7 and 8. As mentioned in Elkins & Eaton (2000), there is no outer peak in the (non-premultiplied) production of $\overline{\phi'^2}$. However, in premultiplied form, the production of $\overline{\phi'^2}$ does develop a second peak in the outer layer, which increases in magnitude and shifts outward with increasing r. This peak occurs at larger z^+ than the growing shoulder in the premultiplied TKE production, which does not develop a distinct peak for the shown profiles. While this does not exclude that an outer peak might appear in k at higher Reynolds num-

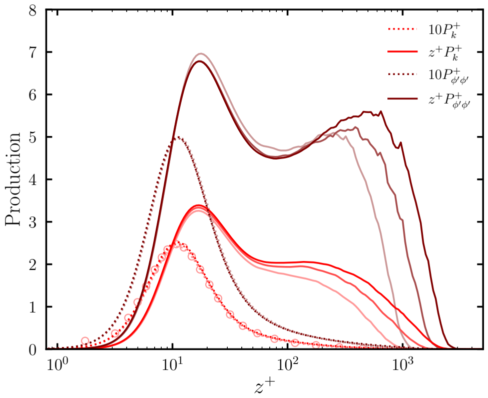

Figure 9. Production and premultiplied production of k and $\overline{\phi'^2}$ in inner units. Line shades correspond to stations described in Figure 7, and the k production from Appelquist *et al.* (2018) for $r = 668$ (○) is provided for comparison.

bers, similar to 2DTBLs (Marusic *et al.*, 2010), it is evident that the strong wake in the mean scalar profile contributes to the emergence of a second peak even at lower Reynolds numbers. This may indicate a fundamental decoupling of momentum and scalar transport in three-dimensional rotating flows, where the velocity field is modified by the crossflow and Coriolis effects that do not directly affect the passive scalar field.

CONCLUSIONS

We have presented a new DNS of the von Kármán 3DTBL for Re_τ up to 2300, reporting the first DNS of its thermal/scalar transport at $Pr = 1$. Comparison of integral and wall quantities from the present DNS to reference data demonstrated good agreement, and the characteristic lack of a wake component was observed in the mean azimuthal velocity profile for profiles up to the disk edge. Confirming experimental observations of Elkins & Eaton (2000), we observe a strong wake component in the mean temperature profile, which persists in magnitude for the radii resolved in the present DNS. Although the scalar variance does not exhibit the second peak observed in the experiments by Elkins & Eaton (2000), it does exhibit a pronounced shoulder in the outer layer, which becomes stronger with increasing r. The high-fidelity dataset collected in the present simulations opens the door to study aspects of relevance for general 3DTBLs, including the differences between momentum and thermal transport via analysis of Reynolds stress and scalar budgets, spectra, and structures.

ACKNOWLEDGMENTS

This work was funded by the Swedish Research Council (Vetenskapsrådet) through the "CATERINA – Centrifugal instability And Turbulence ExpeRIments and Numerical Analyses" project (2021-05587_VR) and by the Erik Petersohn Memorial Foundation. This project received access to the JUPITER supercomputer, funded by the EuroHPC Joint Undertaking, the German Federal Ministry of Research, Technology and Space, and the Ministry of Culture and Science of the German state of North Rhine-Westphalia, via the JUPITER Research and Early Access Program (JUREAP) as part of the EuroHPC project application EHPC-EXT-2024E01-058. Preliminary simulations were performed on the LUMI supercomputer, granted through project NAISS 2025/8-5 from the National Academic Infrastructure for Supercomputing in Sweden (NAISS).

REFERENCES

Alfredsson, P. H., Kato, K. & Lingwood, R. J. 2024 Flows over rotating disks and cones. *Annual Review of Fluid Mechanics* **56**, 45–68.

Appelquist, E., Schlatter, P., Alfredsson, P. H. & Lingwood, R. J. 2018 Turbulence in the rotating-disk boundary layer investigated through direct numerical simulations. *European Journal of Mechanics - B/Fluids* **70**, 6–18.

Bobke, A., Örlü, R. & Schlatter, P. 2016 Simulations of turbulent asymptotic suction boundary layers. *Journal of Turbulence* **17** (2), 157–180.

Digre, D. 2015 The three-dimensional turbulent boundary layer on a rotating disk. Master's thesis, Embry–Riddle Aeronautical University, Daytona Beach, FL.

Dong, S., Karniadakis, G. E. & Chryssostomidis, C. 2014 A robust and accurate outflow boundary condition for incompressible flow simulations on severely-truncated unbounded domains. *Journal of Computational Physics* **261**, 83–105.

Elkins, C. J. & Eaton, J. K. 2000 Turbulent heat and momentum transport on a rotating disk. *Journal of Fluid Mechanics* **402**, 225–253.

Imayama, S., Lingwood, R. J. & Alfredsson, P. H. 2014 The turbulent rotating-disk boundary layer. *European Journal of Mechanics – B/Fluids* **48**, 245–253.

Itoh, M. & Hasegawa, I. 1994 Turbulent boundary layer on a rotating disk in infinite quiescent fluid. *JSME International Journal Series B Fluids and Thermal Engineering* **37** (3), 449–456.

Jansson, N., Karp, M., Podobas, A., Markidis, S. & Schlatter, P. 2024 Neko: A modern, portable, and scalable framework for high-fidelity computational fluid dynamics. *Computers & Fluids* **275**, 106243.

von Kármán, T. 1921 Über laminare und turbulente Reibung. *ZAMM – Zeitschrift für Angewandte Mathematik und Mechanik* **1** (4), 233–252.

Littell, H. S. & Eaton, J. K. 1994 Turbulence characteristics of the boundary layer on a rotating disk. *Journal of Fluid Mechanics* **266**, 175–207.

Lozano-Durán, A., Giometto, M. G., Park, G. I. & Moin, P. 2020 Non-equilibrium three-dimensional boundary layers at moderate Reynolds numbers. *Journal of Fluid Mechanics* **883**, A20.

Marusic, I., Mathis, R. & Hutchins, N. 2010 High Reynolds number effects in wall turbulence. *International Journal of Heat and Fluid Flow* **31** (3), 418–428.

Millsaps, K. & Pohlhausen, K. 1952 Heat transfer by laminar flow from a rotating plate. *Journal of the Aeronautical Sciences* **19** (2), 120–126.

Mollaei, M., Philip, J. & Klewicki, J. C. 2024 An experimental investigation of tangential and radial velocity statistics of a rotating disk boundary layer. In *13th International Symposium on Turbulence and Shear Flow Phenomena*.

Pirozzoli, S. & Orlandi, P. 2021 Natural grid stretching for DNS of wall-bounded flows. *Journal of Computational Physics* **439**, 110408.

Schlatter, P. & Örlü, R. 2012 Turbulent boundary layers at moderate Reynolds numbers: inflow length and tripping effects. *Journal of Fluid Mechanics* **710**, 5–34.

Wu, X. & Squires, K. D. 2000 Prediction and investigation of the turbulent flow over a rotating disk. *Journal of Fluid Mechanics* **418**, 231–264.